Supplementary Information

Excellent antibacterial activities in the dark of ZnO nanoflakes with Oxygen Vacancies on the exposed {$2\bar{1}\bar{1}0$} facets

Ying Zhou‡, Yifan Guo‡, Jinyang Li*, Wei Wei, Dan Li, Lihui Luo, Xiaoling Xu, Zuowan Zhou*.

Key Laboratory of Advanced Technologies of Materials (Ministry of Education), School of Materials Science and Engineering, Southwest Jiaotong University, Chengdu, 610031, China.

*Corresponding authors' E-mail: zwzhou@swjtu.edu.cn, jinyang.li@swjtu.edu.cn

Experimental Details

Materials. Zinc nitrate hexahydrate (Zn $(NO_3)_2 \cdot 6H_2O$) and hexamethylenetetramine (HMTA, $(CH_2)_6N_4$) were purchased from Aladdin Biological Technology Co. Ltd. (Shanghai, China). Sodium hydroxide (NaOH) and ammonia ($NH_3 \cdot H_2O$) were purchased from Chengdu Kelong Chemical Co. Ltd., P. R. China. *E. coli* (ATCC 25922) and *S. aureus* (ATCC 6538) were provided by Guangdong Institute of Microbiology, P. R. China. All other chemicals and materials used in this study were purchased from commercial sources, and were used without further purification.

Preparation of {$2\bar{1}\bar{1}0$}-ZnO and {$10\bar{1}0$}-ZnO. Formation processes of ZnO crystals with different exposed facets are proposed and illustrated in Figure S1. As a functional material, ZnO is one of the richest crystals with diverse morphologies and structures among the family of low-dimensional micro/nano architectures. In the present study, no organic additive or template is introduced into the reaction system, the growth of the ZnO crystals is due to the orientation of polar surface-induced adhesion growth. Thus, in the current Zn $(NO_3)_2$-NaOH system, the OH^- ions are

preferentially enriched on the (0001) polar planes of the ZnO crystals as the chemical environment constantly provides reactants. This variation affects the attachment and growth behaviors of the $Zn(OH)_4^{2-}$ precursor on the (0001) polar surface. In this case, due to the suppression of crystal growth along the [0001] axis, crystal growth along the $[01\bar{1}0]$ direction is relatively enhanced, thus leading to the formation of nanosheets with a high proportion of $\{2\bar{1}\bar{1}0\}$ planes. Subsequently, with some active sites on the surface of nanosheets, $\{2\bar{1}\bar{1}0\}$-faceted flower-like ZnO microstructures are shaped. In the $Zn(NO_3)_2$-$NH_3{\cdot}H_2O$ system, the OH^- and NH_4^+ ions released by $NH_3{\cdot}H_2O$ stabilize the surface charge and the structure of the positively charged Zn-(0001) as well as negatively charged O-(0001) polar surfaces. This variation affects the attachment and growth of the $Zn(OH)_4^{2-}$ precursor, allowing ZnO nanocrystals to grow preferentially along the active direction of the [0001] axis. At the same time, the uncharged molecules of $NH_3{\cdot}H_2O$ tend to attach onto some nonpolar surfaces, which promote the growth of the polar surfaces and can form $\{10\bar{1}1\}$- and $\{10\bar{1}0\}$-faceted urchin-like ZnO.

Computational Methods. First-principles simulation were carried out using CASTEP based on Density functional theory **(**DFT) and plane-waves theory, with the usage of the ultrasoft pseudo potentials. The generalized gradient approximation of Perdew Burke and Ernzerhof, as implemented in the CASTEP package, was employed in the simulation. Dispersion corrected DFT (DFT-D) was applied during the calculation. The size of the periodic supercell for the simulation is 11.26×10.41×24.87 Å for the $\{2\bar{1}\bar{1}0\}$ facet and 13.00×10.41×26.56 Å for the $\{10\bar{1}0\}$ facet, and the vacuum layer height is set as 20 Å. Spin polarization are applied and the initial spin of O atoms in O_2

is set to be triplet in the simulation. The k-point grids are 2× 2× 1 for the calculation, and the cut-off energy for the plane-waves basis set is 400 eV. The convergence tolerance parameters of energy, maximum force, maximum stress, and maximum displacement are 2.0×10^{-5} eV/atom, 0.05 eV/Å, 0.1 GPa, and 0.002 Å, respectively. The adsorption energy (E_{ab}) is given by

$$E_{ab} = E_{ZnO}^{slab} + E_{O2}^{mol} - E_{ZnO-O2}^{slab} \quad (1)$$

Where E_{ZnO}^{slab} means the energy of the crystal facets before adsorbing O_2, E_{O2}^{mol} is the energy of O_2, E_{ZnO-O2}^{slab} means the energy of the crystal facets after adsorbing O_2.

Image Processing Algorithm. Figure 3b displays the geometric relationship of crystal cell parameters, we assume that O'A= a, O'O= c, O'D= dx, n=c/a. So, OD= $(O'O^2+ O'D^2)^{1/2}$, O'C= $y'(x)*$ O'D,

Then, by obtaining the first derivative of the fitting function (2), the $y'(x)$ can be obtained. Taking $dx = 0.003$, and combined with XRD characterization, the ratio of $\{10\bar{1}0\}$ to the total exposed facets area was

$$R_{\{10\bar{1}0\}} = \frac{\sum OC}{\sum OC + \sum OD}. \quad (2)$$

Image analysis technology is applied to fit the data points using Gauss (Figure S4a)), Gauss AMP (Figure S4 (b)), Lorentz (Figure S4c), and Voigt (Figure S4d), respectively. The final fitting equation for Gauss AMP as follows:

$$y = y_0 + Ae^{-\frac{(x-x_c)^2}{2w^2}} \quad (3)$$

Where, x ranging from -3.15 pixel to 3.15 pixel, y_0 is -372711.13492, A is 372783.66361, $2w^2$ is 58137.01503

Characterization. The surface morphologies of the samples were observed by field emission scanning electron microscopy (FE-SEM; Inspect F, FEI, Holland), operated at 20.0 kV. A drop of well-dispersed samples in ethanol water was cast onto a piece of silicon wafer and air-dried. The crystal morphologies were characterized by transmission electron microscopy (TEM; JSM2100F, JEOL, Japan) and the corresponding selected-area electron diffraction (SAED) patterns at an accelerating voltage of 200.0 kV. The samples were prepared by dripping suitable volume of the sample suspension on a copper grid and air-dried. The X-ray diffraction (XRD) patterns were recorded with a Philips X'Pert PRO.

In order to compare the concentration of V_O in ZnO, the equivalent amount of each ZnO sample was put into the same position in the sample chamber of Electron paramagnetic resonance (EPR) spectrometer. EPR spectra were measured at 77 K by Broker EMX 500 EPR spectrometer.

The amount of $\cdot O_2^-$ and H_2O_2 in absence of light H_2O_2 generated from aqueous ZnO suspensions was estimated by KI redox titrations [1]. H_2O_2 generated from ZnO suspension was determined by measuring the absorbance at 580 nm by UV-visible spectrophotometer (UV-2550, Shimadzu, Japan) at 0, 0.5, 1, 1.5, 2, 3 and 4 h, respectively. $\cdot O_2^-$ from aqueous suspensions of ZnO were estimated by nitro blue tetrazolium (NBT)[2]. Standard curve between the absorbance and concentration of H_2O_2 was shown in Figure S7. UV-vis spectrophotometer was also used to detect the

absorbance of different concentrations of NBT solution at 306.5 nm (as shown in Figure S8). According to the relationship between the concentration of NBT standard solution and its corresponding absorbance, a standard curve was drawn (Figure S9 Show).However, after a series of experiences were carried out to investigate ZnO crystals with the exposed facets' production of ROS, we monitored the production of $\cdot O_2^-$ and H_2O_2 in suspension of the as-mentioned ZnO was detected without any light irradiation.

Evaluation of antibacterial activity. The antibacterial activities of the as-prepared samples were tested by the mean colony-forming unit's method and the minimum inhibitory concentration (MIC) measurement. The antibacterial ratio was determined according to the mean colony-forming units method proposed by Xu *et al*[1a]. Each test was repeated three times. The antibacterial ratio was determined by using the following equation:

$$\text{Antibacterial ratio} = \frac{N_0 - N}{N_0} \times 100\% \quad (4)$$

Where, N_0 is the mean number of living bacteria in the control sample, and N is the mean number of living bacteria in the testing sample.

To compare with other antibacterial agents, the MIC values of the as-prepared ZnO samples were tested. The reported data were the average value of three parallel runs in Figure 2 and Figure S7.

It has been well-known that the antibacterial activity of ZnO might be originated from zinc ions released [3] and the photocatalysis as mentioned. As shown in Figure.

S13 and Figure. S14, the results prove that the leaching of zinc ions is not enough to be considered as a contributing effect.

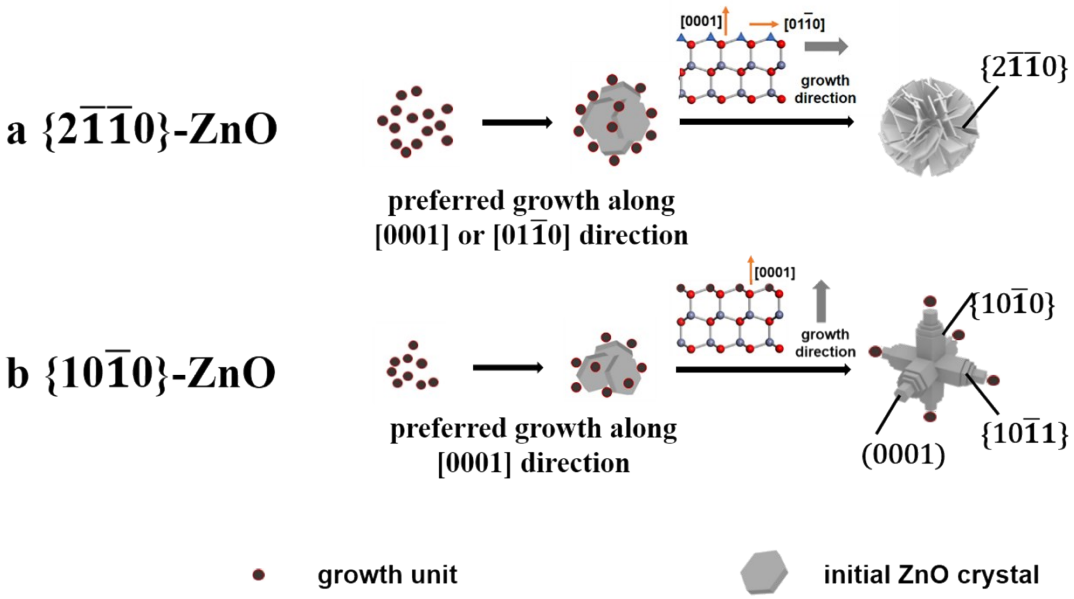

Figure S1. Schematic diagram of the growth of ZnO crystals with different exposed facets. a) {2$\bar{1}\bar{1}$0}-ZnO and b) {10$\bar{1}$0}-ZnO.

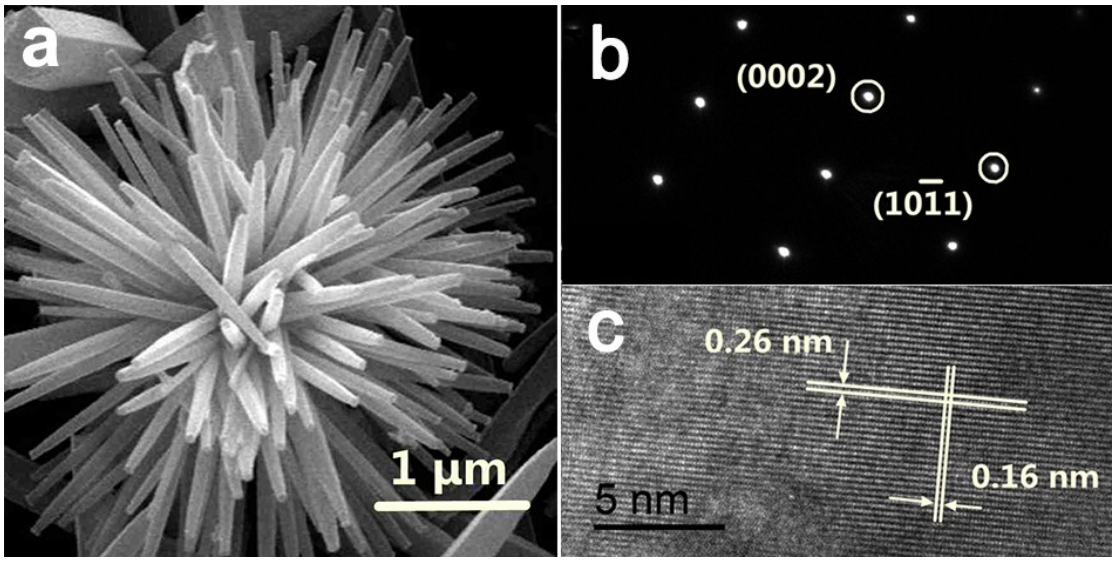

Figure S2. Morphology characterization of $\{10\bar{1}0\}$-ZnO. a) SEM image, b) SAED pattern and c) HR-TEM image.

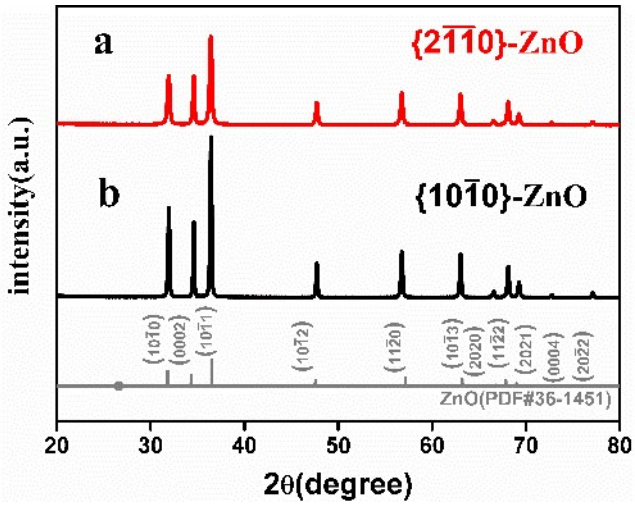

Figure S3. XRD patterns of ZnO crystals of a) $\{2\bar{1}\bar{1}0\}$-ZnO and b) $\{10\bar{1}0\}$-ZnO.

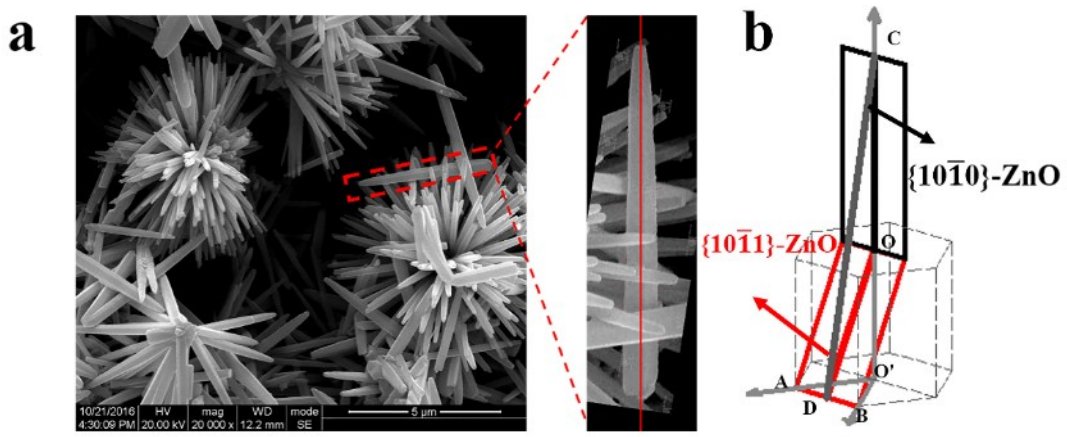

Figure S4. a) SEM image processing algorithm of a single needle of $\{10\bar{1}0\}$-ZnO. b) Math model for calculating the ratio of exposed facets on the urchin-like ZnO needle.

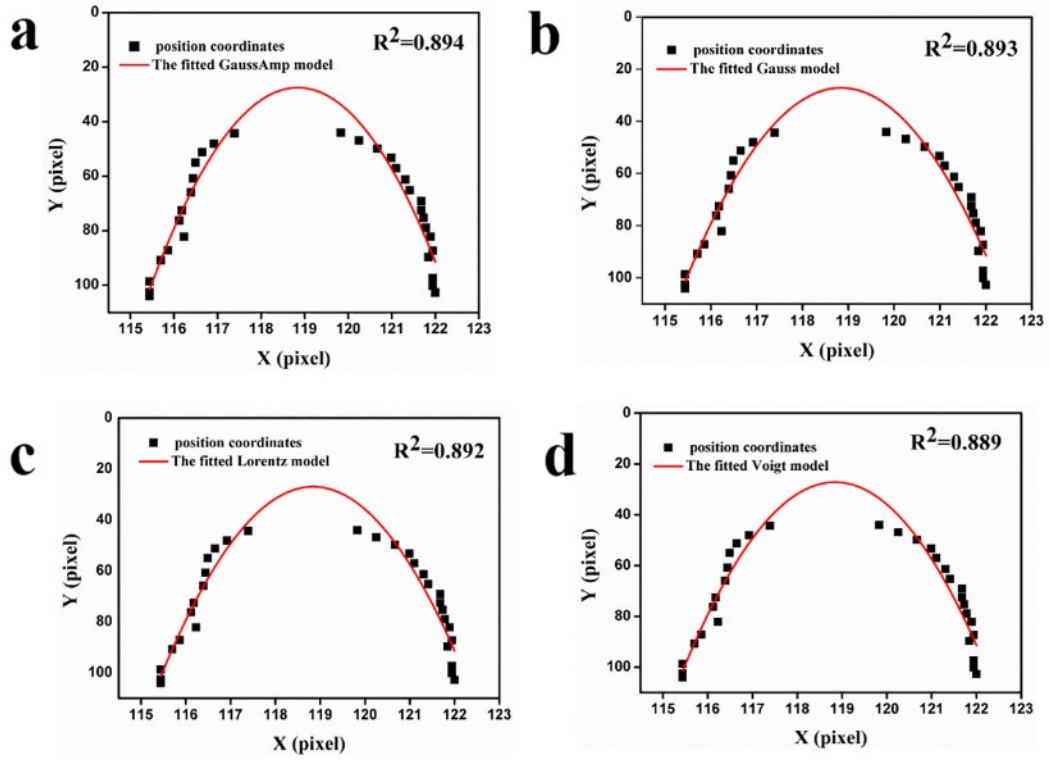

Figure S5. Fitting curves of uniform points using a) Gauss fitting, b) Gauss AMP fitting, c) Lorentz fitting, d) Voigt fitting.

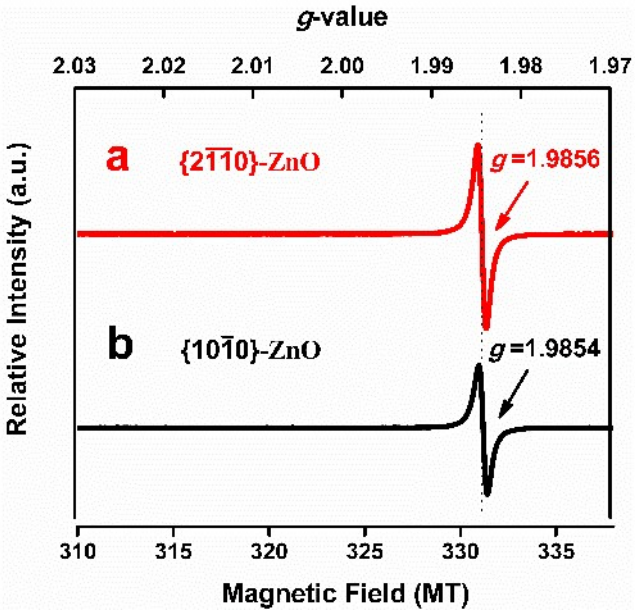

Figure S6. The OVs of the two kinds of ZnO exposed facets are determined by EPR. a) {$2\bar{1}\bar{1}0$}-ZnO and b) {$10\bar{1}0$}-ZnO.

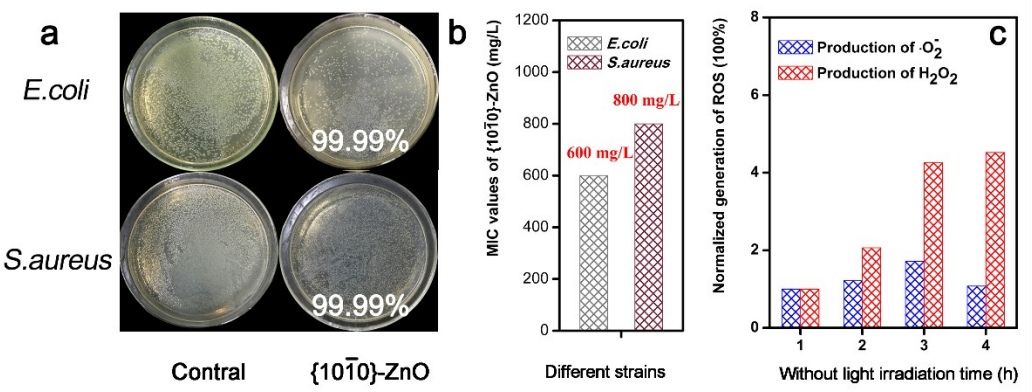

Figure S7. The antibacterial activities against *E. coli* and *S. aureus* of a) colony count, b) the minimal inhibit concentration (MIC) values and c) normalized generation of $\cdot O_2^-$ and H_2O_2 produced by $\{10\bar{1}0\}$-ZnO in dark.

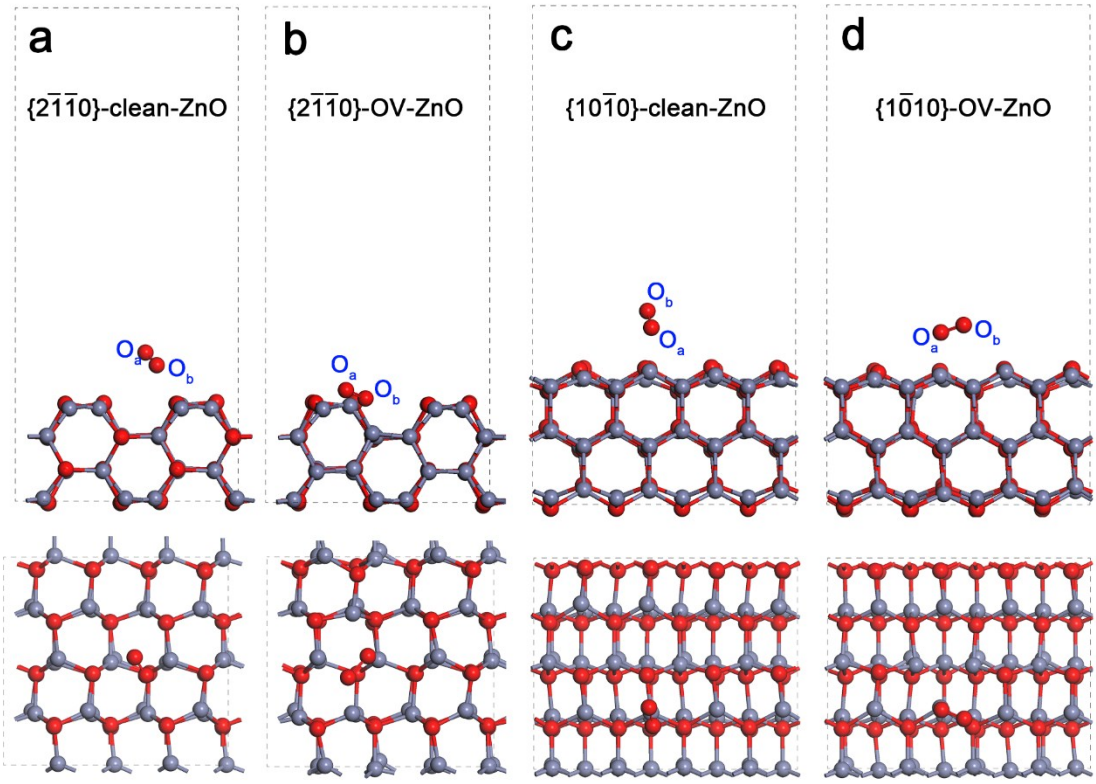

Figure S8. The optimized structure of O_2 adsorbed on the ZnO surfaces. a) $\{2\bar{1}\bar{1}0\}$-clean-ZnO, b) $\{2\bar{1}\bar{1}0\}$-OV-ZnO, c) $\{10\bar{1}0\}$-clean-ZnO, d) $\{10\bar{1}0\}$-OV-ZnO.

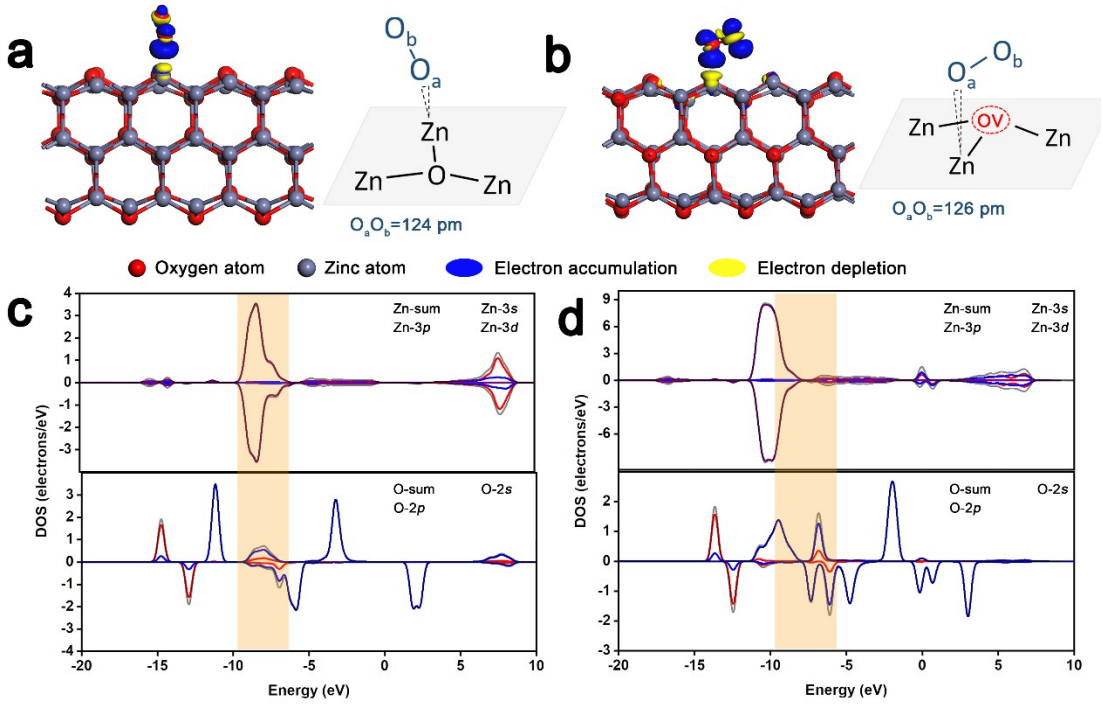

Figure S9. The electron density difference maps of O_2 adsorbed on the a) clean regions and b) OVs regions of $\{10\bar{1}0\}$-ZnO, The blue and yellow represent electron accumulation and depletion with an isovalue=0.002 a.u. Density of states (DOS) of the adsorbed oxygen and neighboring Zn atoms on c) $\{10\bar{1}0\}$-clean-ZnO and d) $\{10\bar{1}0\}$-OV-ZnO.

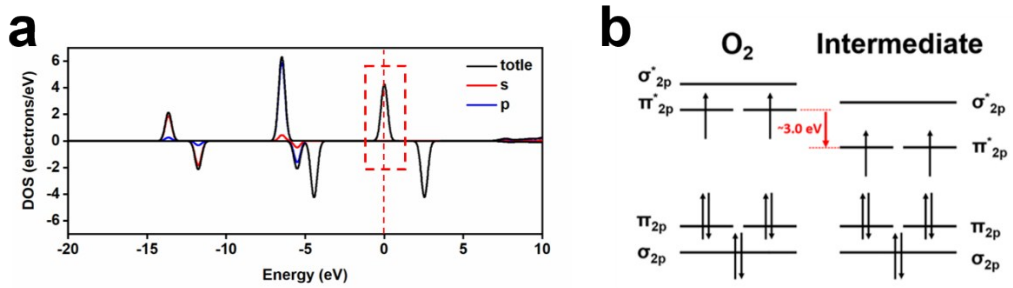

Figure S10. Electronic structure of O_2 molecule and intermediate. a) DOS of O_2, the red dot indicate the fermi level and the red rectangle refers to the π^*_{2p} orbital of O_2. b) The molecular orbital diagram of O_2 and intermediate.

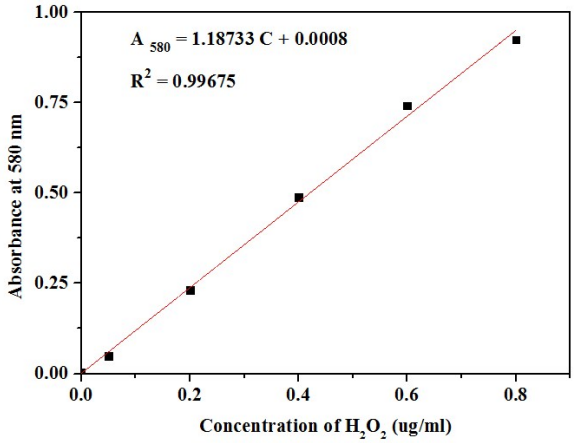

Figure S11. Standard curve fitting from UV-visible absorption spectra characterized with specific concentration of H_2O_2.

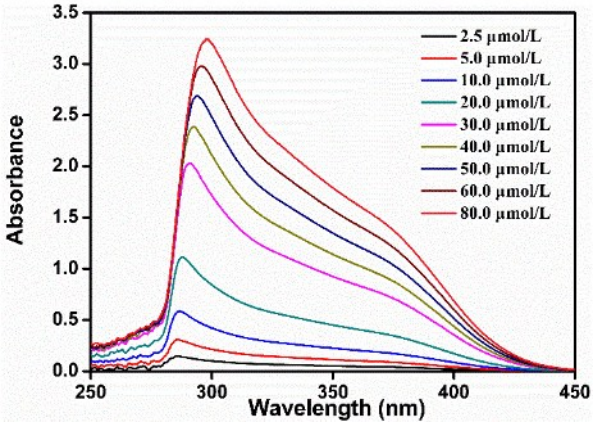

Figure S12. UV-visible absorption spectra of ZnO suspension containing different concentration of NBT in the absence of light.

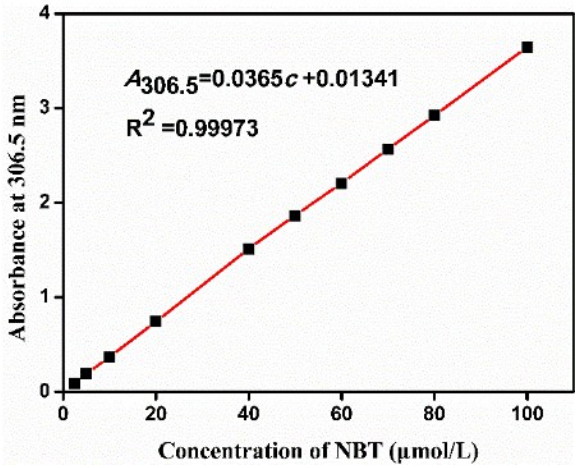

Figure S13. Relationship between the absorbance at 306.5nm and the concentration of NBT.

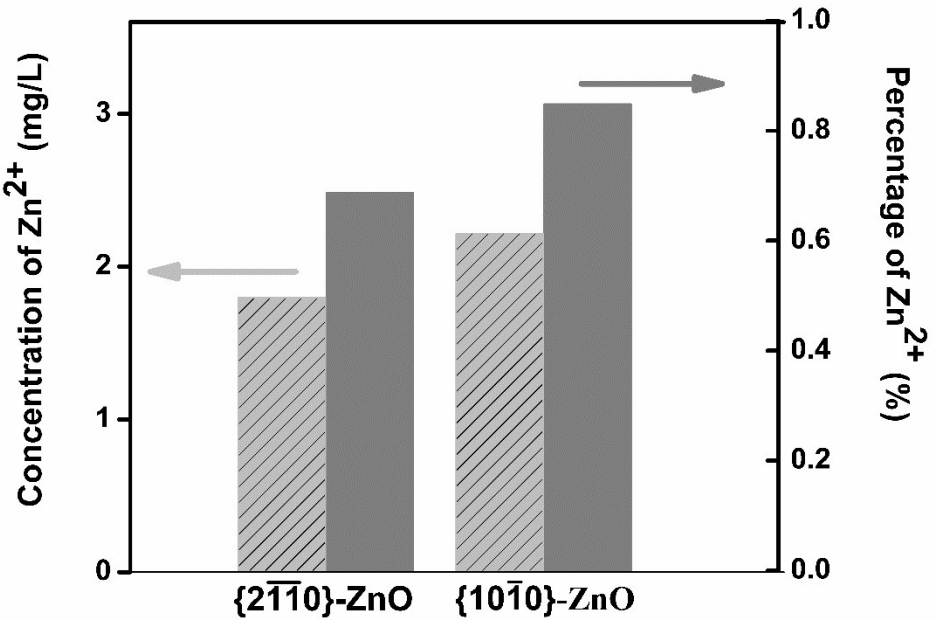

Figure S14. Concentration of Zn^{2+} in the ZnO suspension of $\{2\bar{1}\bar{1}0\}$-ZnO and $\{10\bar{1}0\}$-ZnO. Concentration of Zn^{2+} is measured in the aqueous suspensions of 500 mg/L ZnO. Percentage of Zn^{2+} = (A/B) × 100%, where A is the concentration of Zn^{2+} and B is the corresponding concentration of ZnO.

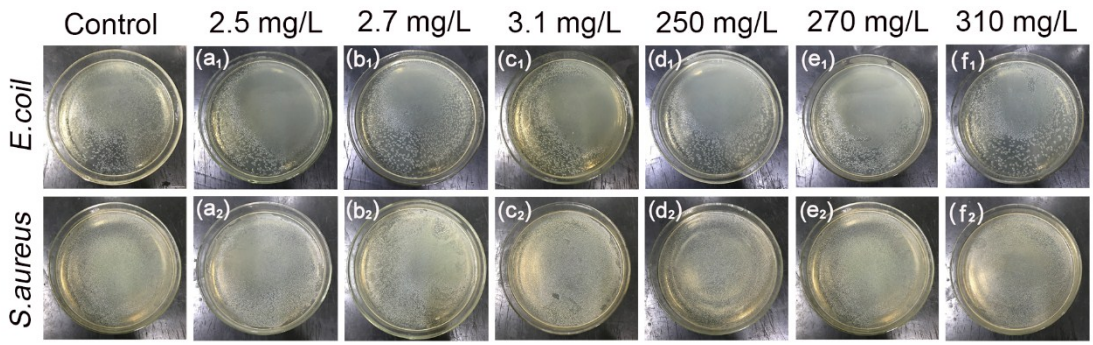

Figure S15. Colony count of *E. coli* and *S. aureus* after 24 h incubation at 37 °C. The bacterial suspension was added with different concentrations of Zn^{2+} in the beginning. (a_1, a_2) 2.5 mg/L, (b_1, b_2) 2.7 mg/L, (c_1, c_2) 3.1 mg/L, (d_1, d_2) 250 mg/L, (e_1, e_2) 270 mg/L and (f_1, f_2) 310 mg/L, which clearly shows that there are no antibacterial activities in the samples with no matter the similar concentration or the 100 times higher concentration of Zn^{2+} that were detected in the aqueous suspension of $\{2\bar{1}\bar{1}0\}$-ZnO and $\{10\bar{1}0\}$-ZnO.

[1] aX. Xu, D. Chen, Z. Yi, M. Jiang, L. Wang, Z. Zhou, X. Fan, Y. Wang, D. Hui, *Langmuir* **2013**, *29*, 5573-5580; bY. Wolanov, P. V. Prikhodchenko, A. G. Medvedev, R. Pedahzur, O. Lev, *Environ Sci Technol* **2013**, *47*, 8769-8774.

[2] H. Goto, *Journal of Catalysis* **2004**, *225*, 223-229.

[3] aA. Joe, S.-H. Park, K.-D. Shim, D.-J. Kim, K.-H. Jhee, H.-W. Lee, C.-H. Heo, H.-M. Kim, E.-S. Jang, *Journal of Industrial and Engineering Chemistry* **2017**, *45*, 430-439; bA. I. B. Christopher J. Frederickson1, *Biometals* **2001**, *14*, 353–366.